

Multiplexed absorption tomography with calibration-free wavelength modulation spectroscopy

Weiwei Cai (蔡伟伟) and Clemens F. Kaminski^{a)}

Department of Chemical Engineering and Biotechnology, University of Cambridge, Cambridge CB2 3RA, United Kingdom

(Received 17 March 2014; accepted 6 April 2014; published online 17 April 2014)

We propose a multiplexed absorption tomography technique, which uses calibration-free wavelength modulation spectroscopy with tunable semiconductor lasers for the simultaneous imaging of temperature and species concentration in harsh combustion environments. Compared with the commonly used direct absorption spectroscopy (DAS) counterpart, the present variant enjoys better signal-to-noise ratios and requires no baseline fitting, a particularly desirable feature for high-pressure applications, where adjacent absorption features overlap and interfere severely. We present proof-of-concept numerical demonstrations of the technique using realistic phantom models of harsh combustion environments and prove that the proposed techniques outperform currently available tomography techniques based on DAS. © 2014 Author(s). All article content, except where otherwise noted, is licensed under a Creative Commons Attribution 3.0 Unported License. [<http://dx.doi.org/10.1063/1.4871976>]

Laser absorption spectroscopy has become a ubiquitous tool for combustion scientists due to its ease of implementation, species-selectivity, capability of measuring both scalar and vector flow parameters (i.e., temperature, species concentration, pressure, and velocity),^{1,2} and high-sensitivity when combined with cavity enhanced/ring-down spectroscopy (CEAS/CRDS),^{3–6} wavelength modulation spectroscopy (WMS),^{7,8} or photoacoustic spectroscopy.⁹ Over the past decades, absorption spectroscopy has been empowered by significant advances and reduced costs of lasers, detectors, and data acquisition systems and matured into a flexible and sensitive technique. For example, the advent of high brightness ultra-high bandwidth supercontinuum sources has led to a paradigm shift in multiplexed absorption spectroscopy, permitting temperature, and concentration of multiple species to be measured simultaneously from spectra covering more than one octave in the near-infrared.^{3–5,10–13} It was further demonstrated that in combination with time-of-flight detection schemes,^{10,13} temporal resolution approaching MHz repetition rates can be achieved. However, all of the mentioned techniques suffer one major drawback in that they are line-of-sight (LOS) techniques incapable of recovering spatially resolved information along the laser beam axis, a critical limitation hampering their application in non-uniform flows. To enable spatial resolution, much research effort is currently directed at combining LOS techniques with tomographic methods and thus to recover the spatial distribution of molecular absorbance. If two, or more, suitable absorption transitions are measured with tomographic absorption spectroscopy, it is possible to recover temperature and concentration information simultaneously for each sample co-ordinate from absorbance ratios.¹⁴ Typically in tomography, one records data along numerous viewing angles (projections), each of which contains multiple LOS measurements. Displacement of these projections inevitably requires an angular sweep of the beam, which undermines

the temporal resolution of the tomographic technique, making it impractical to trace transient phenomena in turbulent flames. Since traditional tomography results in a set of linear equations, we refer to it here as *linear* tomography. Recently, a tomographic technique based on supercontinuum enabled absorption spectroscopy was proposed by our group, which can take full advantage of the enormous spectral bandwidth provided and is capable of imaging not only temperature and species concentration but also pressure distributions in fluctuating environments.¹⁵ In difference to *linear* tomography, which intensively samples only the spatial dimension, the latter approach manages to incorporate an additional (i.e., spectral) dimension and the algorithm recovers distributions of the independent variables (i.e., temperature and species concentration) directly. Since projections are nonlinearly dependent on those parameters, a system of nonlinear equations is obtained, and we refer to this as *nonlinear* tomography. We demonstrated that two fixed orthogonal projections are sufficient for the reconstruction processes in *nonlinear* tomography, not only reducing experimental cost but also increasing temporal resolution into the MHz domain.

Unfortunately, all previously mentioned tomographic concepts were based on the direct absorption spectroscopy (DAS); hence, disadvantages inherent to DAS are also inherited by their tomographic counterparts. WMS, on the other hand, does not suffer these drawbacks and enjoys three critical advantages compared to DAS,¹⁶ including: (1) improved sensitivity because of inherently better (10–100×) signal-to-noise ratios (SNRs) as low-frequency noise is effectively suppressed when detecting harmonics of the modulation frequency; (2) resistance to laser intensity fluctuation induced by, e.g., soot or dust scattering and system vibration; and (3) exemption from baseline fitting requirements, essential for, but difficult to achieve, in DAS applied to high pressure scenarios, where neighboring absorption features interfere severely.^{5,15} WMS has been extensively adopted for industrial applications due to the low cost of tunable diode laser

^{a)}Electronic mail: cfk23@cam.ac.uk



sources and broad wavelength selectivity (diode lasers for the near-infrared and quantum cascade lasers for mid-infrared and far-infrared),^{17,18} and narrow linewidth (sub-MHz), etc. Compared with supercontinuum radiation, tunable semiconductor lasers can be easily wavelength tuned at speed and they can be modulated with almost linear response via variation in injection current. Nonetheless, like its DAS counterpart, WMS has so far been limited by its LOS nature and only uniform flames have been probed whose surroundings were purged with non-absorbing gas to reduce interference from ambient absorption. This motivates us to combine the advantages of *nonlinear* tomography with calibration-free WMS using tunable semiconductor lasers, pushing the application limit of absorption-based tomographic techniques to harsh combustion environments such as coal-fired power plant boilers filled with flying ashes and in-flight engine monitoring suffering from vibration, etc.

Here, we develop the theoretical framework for WMS-based multiplexed absorption tomography (MAT) and show that this gives calibration-free, spatially resolved information on flow scalars, at improved resolution and reduced sensitivity to noise. As WMS with tunable semiconductor lasers has been extensively discussed in the literatures before,^{19,20} we here summarize only basic concepts as necessary to develop the nonlinear MAT algorithm. The wavelength modulation is simply realized by imposing a high-frequency sinusoidal modulation on the laser injection current, resulting in laser frequency variations as

$$\nu(t) = \bar{\nu} + a \cos(2\pi f_m t), \quad (1)$$

where $\bar{\nu}$ is the line-center frequency; and f_m and a are the modulation frequency and depth, respectively. The corresponding laser intensity modulation can be described by

$$I(t) = \bar{I}_0 \cdot [1 + i_0 \cos(2\pi f_m t + \psi_1) + i_2 \cos(4\pi f_m t + \psi_2)], \quad (2)$$

where \bar{I}_0 is the average laser intensity at the line-center; i_0 and i_2 are the linear and nonlinear modulation amplitudes; and ψ_1, ψ_2 are the corresponding phase shifts with respect to frequency modulation. For small a , e.g., $a < 0.1 \text{ cm}^{-1}$, i_2 is negligible, and in this case, the laser intensity scales linearly with driving current.

According to the Beer-Lambert law, the transmission coefficient of a monochromatic light beam with frequency of ν passing through *non-uniform* absorbing medium is defined as

$$\begin{aligned} \tau(\nu) &= \exp[-\alpha(\nu)] \\ &= \exp \left\{ - \int_{L_1}^{L_2} \sum_g S[T(l), \nu_g] \cdot \phi[T(l), X(l), \nu] \right. \\ &\quad \left. \times P \cdot (\nu_g - \nu) \cdot P \cdot X(l) \right\}, \end{aligned} \quad (3)$$

where α stands for the absorbance; L_1 and L_2 are the intersections between the laser beam and the boundaries of the region of interest (ROI); $T(l)$ and $X(l)$ are the temperature and concentration profiles along the LOS as a function

of distance l , respectively; ϕ is the normalized Voigt line-shape function which approximates the convolution of the two dominant broadening mechanisms (Doppler and collisional); and $S[T(l), \nu_g]$ is the line strength of the g th non-negligible transition centered at ν_g and at temperature $T(l)$. For normal LOS experiments, it has to be noted that $T(l)$ and $X(l)$ are assumed to be constant for spatially averaged measurement.

Since $\tau(t)$ is an even function with respect to t , it can be expanded as Fourier cosine series

$$\tau(\bar{\nu} + a \cos(\omega t)) = \sum_{k=0}^{\infty} H_k(\bar{\nu}, a) \cos(k\omega t), \quad (4)$$

where H_k represents the k th order harmonic coefficient which can be calculated as

$$H_0(\bar{\nu}, a) = \frac{1}{2\pi} \int_{-\pi}^{\pi} \tau(\bar{\nu} + a \cos \theta) d\theta, \quad (5)$$

$$H_k(\bar{\nu}, a) = \frac{1}{\pi} \int_{-\pi}^{\pi} \tau(\bar{\nu} + a \cos \theta) \cos k\theta d\theta. \quad (6)$$

The 1st and 2nd harmonics of the signal (denoted by S_{2f} and S_{1f}) can then be calculated if the laser parameters, i.e., i_0, i_2, ψ_1, ψ_2 , and a are known via Eqs. (7) and (8)

$$\begin{aligned} S_{2f} &= \frac{G\bar{I}_0}{2} \left\{ \left[H_2 + \frac{i_0}{2}(H_1 + H_3) \cos \psi_1 + i_2 \left(H_0 + \frac{H_4}{2} \right) \cos \psi_2 \right]^2 \right. \\ &\quad \left. + \left[\frac{i_0}{2}(H_1 - H_3) \sin \psi_1 + i_2 \left(H_0 - \frac{H_4}{2} \right) \sin \psi_2 \right]^2 \right\}^{1/2}, \end{aligned} \quad (7)$$

$$\begin{aligned} S_{1f} &= \frac{G\bar{I}_0}{2} \left\{ \left[H_1 + i_0 \left(H_0 + \frac{H_2}{2} \right) \cos \psi_1 + \frac{i_2}{2}(H_1 + H_3) \cos \psi_2 \right]^2 \right. \\ &\quad \left. + \left[i_0 \left(H_0 - \frac{H_2}{2} \right) \sin \psi_1 + \frac{i_2}{2}(H_1 - H_3) \sin \psi_2 \right]^2 \right\}^{1/2}. \end{aligned} \quad (8)$$

Here, G is a scaling factor accounting for both the optical and electrical gains of the detection system and transmission losses caused by scattering, reflections, beam steering, window fouling, etc. By taking the ratio of Eqs. (7) and (8), the pre-factor cancels out. The result, labeled as $S_{2f/1f}$, defines the 1f-normalized, 2f signal that provides a calibration-free measurement unaffected by G . The normalized signal thus only depends on laser parameters and absorber properties (i.e., temperature and concentration). Phase shifts ψ_1 and ψ_2 , amplitudes i_0 and i_2 for the laser source are conveniently determined using the method outlined in Ref. 21. Hence, the LOS-averaged gas properties can be directly inferred by fitting measurement data with the model detailed above, and avoiding any need for calibration, which is often impossible in harsh, practical environments. This method has been extensively validated and is explained in more detail in Refs. 19, 22, and 23. Here, we take Eqs. (7) and (8) as the starting point for the development of WMS-based nonlinear tomography, which overcomes the limitation of LOS techniques.

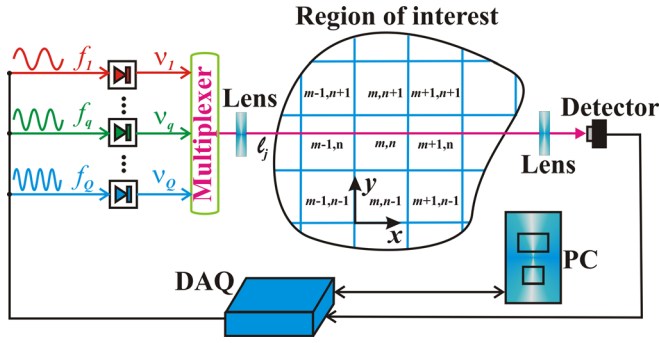


FIG. 1. Illustration of the multiplexed absorption tomography based on the calibration-free wavelength modulation spectroscopy.

Figure 1 illustrates how the techniques are implemented in principle and the corresponding mathematical formulation. Multiple laser diodes are used to probe the target species at the line centers of transitions q , at frequency ν_q , and their output is combined using a wavelength multiplexer. Each of the diodes is modulated at a frequency that is different from the others so that its harmonic signals can be differentiated using lock-in amplifiers. The multiplexed laser source can then be either split into multiple beams to map out the ROI, or, it is laterally translated across the ROI in a step-wise fashion at a cost of reduced temporal resolution. As illustrated in Fig. 1, a beam at the j th measurement location, ℓ_j , is attenuated on passage through the ROI by sample absorption, and picked up by a photo detector. The registered signal is digitized and post-processed using a lock-in detection algorithm, implemented in software, to recover the harmonic signals. This recovers Q nonlinear equations for $S_{2f/1f}$ at each ℓ_j , where Q corresponds to the number of laser diodes used. Each $S_{2f/1f}$ is a function of temperature and species concentration along the LOS. Thus, mapping out the ROI over all locations ℓ_j and probing Q transitions in each location one obtains a system of $\ell_j \times Q$ coupled nonlinear equations (*nonlinear tomography*). To approximate solutions to

this, we transform the equations into an optimization problem with an objective function defined as

$$F = D + \gamma_T \cdot R_T(\bar{T}^{trial}) + \gamma_X \cdot R_X(\bar{X}^{trial}),$$

$$D = \sum_{j=1}^J \sum_{i=1}^I \left[1 - S_{2f/1f}^c(\ell_j, \lambda_i, \bar{T}^{trial}, \bar{X}^{trial}) / S_{2f/1f}^m(\ell_j, \lambda_i) \right]^2, \quad (9)$$

where indices i and j run through all the probed transitions and measurement locations, respectively; \bar{T}^{trial} and \bar{X}^{trial} are the trial distributions for temperature and concentrations; R_T and R_X are the regularization terms, which can be used to enforce *a priori* information such as smoothness. They are defined in Eq. (10) and have weighting factors γ_T and γ_X , respectively. $S_{2f/1f}^c$ and $S_{2f/1f}^m$ are the calculated and measured $1f$ -normalized, $2f$ signals, respectively. The optimization problem can then be solved by a global optimizer such as the simulated annealing (SA) algorithm²⁴⁻²⁷

$$R_T(\bar{T}^{rec}) = \sum_{m=1}^M \sum_{n=1}^N \left[\left(\sum_{i=m-1}^{m+1} \sum_{j=n-1}^{n+1} |T_{ij}^{rec} - T_{m,n}^{rec}| \right) / 8 \right]^2,$$

$$R_X(\bar{X}^{rec}) = \sum_{m=1}^M \sum_{n=1}^N \left[\left(\sum_{i=m-1}^{m+1} \sum_{j=n-1}^{n+1} |X_{ij}^{rec} - X_{m,n}^{rec}| \right) / 8 \right]^2. \quad (10)$$

Panel (a) in Fig. 2 presents example absorption spectra for different pressure conditions for H_2O , representing the major species produced in hydrocarbon/hydrogen flames. It is clearly evident how the absorption lineshape broadens with increasing pressure. For DAS, this is a detrimental attribute as, in contrast to WMS, baseline fitting is required for quantification. At high pressure, this becomes a prohibitive problem. Panel (b), on the other hand, shows the

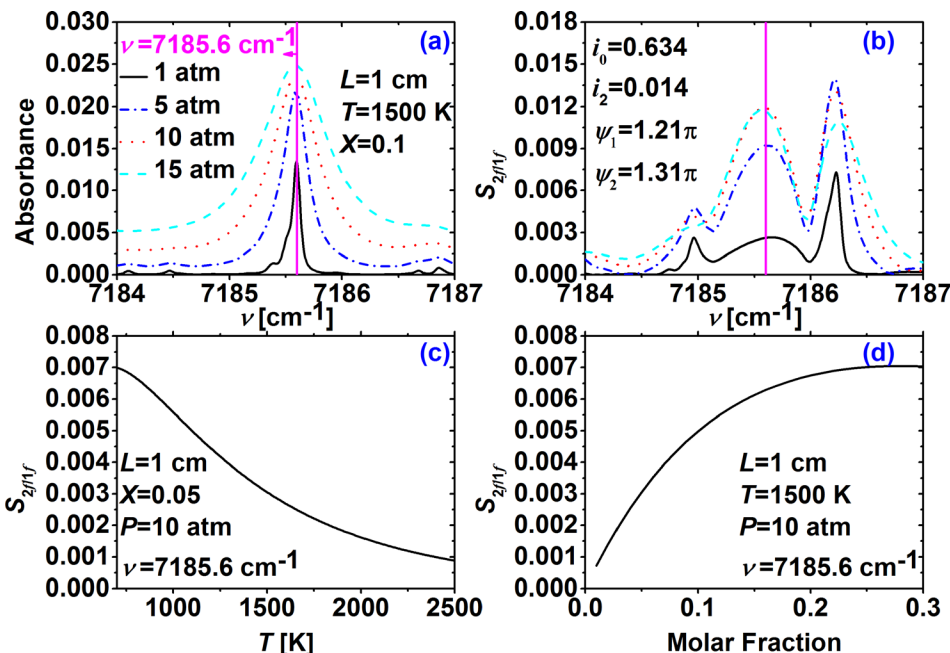


FIG. 2. (a) and (b) Example signals for DAS and WMS, respectively; (c) and (d): $1f$ -normalized, $2f$ signals as a function of temperature and water vapor concentration, respectively.

corresponding $S_{2f/1f}$ signals, simulated for the indicated laser parameters. The molecular transitions are now represented by multiple peaks and their appearance differs significantly from those obtained by direct absorption (panel (a)) since the signal now is proportional to curvature of the spectrum rather than intensity. Panels (c) and (d) show how the $S_{2f/1f}$ signal at center wavelength (7185.6 cm^{-1}) responds within the range of temperature and concentration typically encountered in practical flames. We note that, unlike absorbance, which for small concentrations varies in a linear fashion with concentration, the $1f$ -normalized, $2f$ signal responds nonlinearly.

As a proof-of-concept demonstration of the nonlinear MAT, two sets of phantom groups, each containing multimodal distributions of temperature and water vapor concentration, are depicted in Fig. 3. The pressure is assumed to be 10 atm and uniform across the ROI. The phantoms are meshed into 15×15 pixels that provide sufficient resolution to reveal the major features of the phantoms. We perform the simulations with five H_2O transitions in the near-infrared spectral range that can be targeted by standard, telecommunication-grade, tunable diode lasers. For details on how to select optimal transitions for WMS, the reader is referred to Ref. 22. In the simulations, the ROI is probed at 30 locations l_j , using 15 beams each along the x and y axes, respectively (see Fig. 1). This yields a plane across the ROI with 15×15 resolution elements. A forward simulation was carried out for all transitions and locations from the phantom distribution such as to obtain idealized versions for $S_{2f/1f}$. Gaussian noise was then added with amplitude of 5% to the line center signal to present various imperfections such as beam steering, non-ideal optics, and etalon fringing. Since beam at l_j contribute $Q = 5$ nonlinear equations, totaling 150 equations to solve for 450 variables (225 for \bar{T} and 225 for \bar{X}) requires use of the smoothness conditions.

Example reconstructions are shown in panels (a) and (c) of Fig. 4; corresponding error contours are shown in panels (b) and (d). We note that the weighting factors γ_T and γ_X in Eq. (9) play an important role to ensure that the model

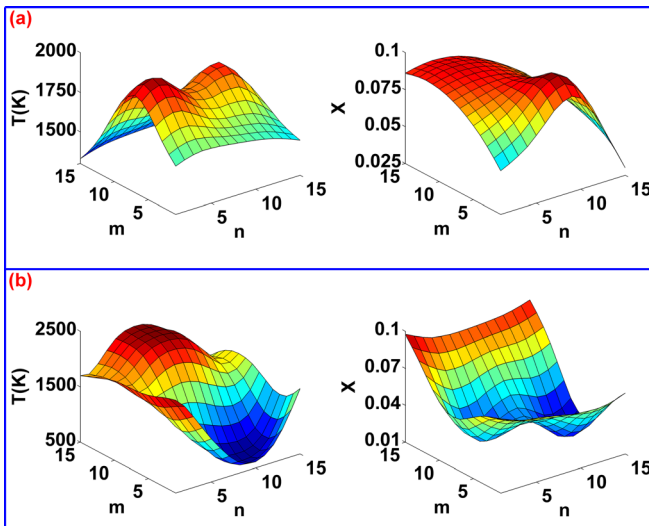


FIG. 3. Phantom distributions of temperature and water vapor concentration to mimic practical flames²⁸ in a numerical demonstration of the algorithm.

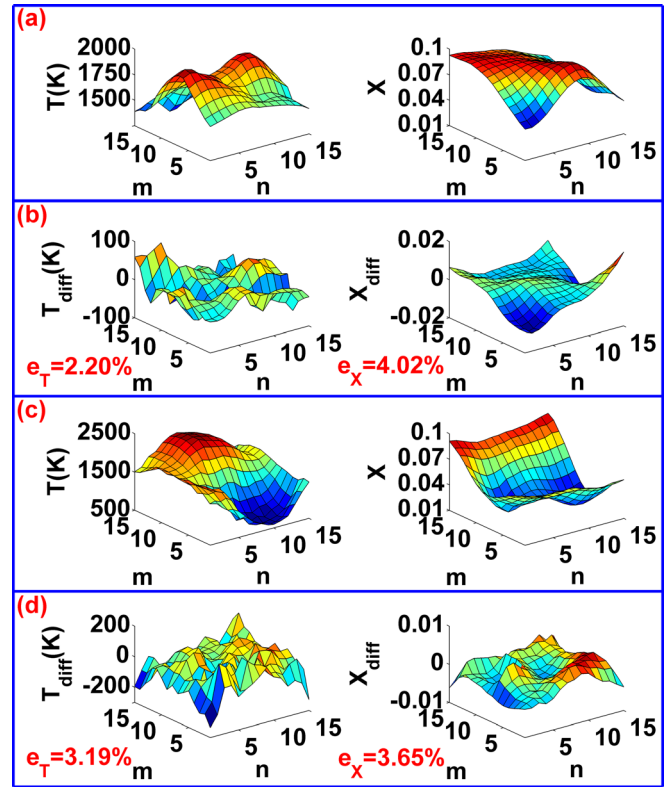


FIG. 4. Reconstructions for two phantom groups with 5% Gaussian noise added to the $1f$ -normalized, $2f$ signals.

represents an acceptable fit to the WMS MAT-data on one hand, and that the smoothness condition is satisfied on the other. The balance between smoothness and goodness of fit determines whether error contours appear “smooth,” as for the example seen for the concentration error contour shown in panel (b), or “noisy,” as is the case for all other error contours shown. For details on the selection of proper weighting factors for regularized optimization problems, the readers are referred to Refs. 29 and 30. The overall performance of the reconstruction algorithm is quantified in the figure via the fractional temperature and concentration errors e_T and e_X , respectively

$$\begin{aligned} e_T &= \left\| \bar{T}^{\text{rec}} - \bar{T}^{\text{true}} \right\|_1 / \left\| \bar{T}^{\text{true}} \right\|_1, \\ e_X &= \left\| \bar{X}^{\text{rec}} - \bar{X}^{\text{true}} \right\|_1 / \left\| \bar{X}^{\text{true}} \right\|_1, \end{aligned} \quad (11)$$

where superscripts distinguish between phantoms (“true”) and reconstructions (“rec”); $\| \cdot \|_1$ denotes the Manhattan norm. Even in the presence of significant levels of noise (5% on the $1f$ -normalized, $2f$ signals), the reconstructions faithfully recover the original phantoms with average temperature errors of only ~ 50 K. This is a remarkable improvement over DAS based tomography, whose achievable SNR are typically $10\text{--}100\times$ less than those with WMS. For the pressure, temperature, and noise conditions presently simulated, DAS would be incapable of recovering the original absorber concentrations and temperatures.

In summary, this paper proposes a *nonlinear* tomographic technique that incorporates the advantages of calibration-free and high sensitivity WMS with tunable semiconductor lasers and is capable to recover precisely the

distributions of species concentration and temperature in hostile environments. The technique is significantly more immune to noise compared to methods based on DAS, and is thus, like standard WMS, ideally suited for applications in harsh technical combustion environments. There is no theoretical penalty in speed compared to standard WMS (if all beams are delivered simultaneously across the different l_j) and thus MHz sensor bandwidth³¹ with spatial resolution is achievable. We anticipate applications in harsh and dynamic technical combustion systems, such as soot-laden incineration plants, coal-fired power plants, and industrial furnaces such as used in steel mills. In contrast to currently available methods, MAT recovers vital localized information on process “hotspots,” inefficiencies and pollutant formation.

This work was funded by the European Commission under Grant No. ASHTCSC 330840 and was performed using the Darwin Supercomputer of the University of Cambridge High Performance Computing Service.

¹F. Li, X. Yu, W. Cai, and L. Ma, *Appl. Opt.* **51**, 4788–4797 (2012).

²M. G. Allen, *Meas. Sci. Technol.* **9**, 545–562 (1998).

³T. Laurila, I. Burns, J. Hult, J. Miller, and C. Kaminski, *Appl. Phys. B* **102**, 271–278 (2011).

⁴J. Langridge, T. Laurila, R. Watt, R. Jones, C. Kaminski, and J. Hult, *Opt. Express* **16**, 10178–10188 (2008).

⁵R. S. Watt, T. Laurila, C. F. Kaminski, and J. Hult, *Appl. Spectrosc.* **63**, 1389–1395 (2009).

⁶Z. Qu, J. Engstrom, D. Wong, M. Islam, and C. F. Kaminski, *Analyst* **138**, 6372–6379 (2013).

⁷G. B. Rieker, J. B. Jeffries, and R. K. Hanson, *Appl. Opt.* **48**, 5546–5560 (2009).

⁸H. Li, G. B. Rieker, X. Liu, J. B. Jeffries, and R. K. Hanson, *Appl. Opt.* **45**, 1052–1061 (2006).

⁹K. Tennal, G. J. Salamo, and R. Gupta, *Appl. Opt.* **21**, 2133–2140 (1982).

¹⁰R. Watt, C. Kaminski, and J. Hult, *Appl. Phys. B* **90**, 47–53 (2008).

¹¹J. Hult, R. S. Watt, and C. F. Kaminski, *Opt. Express* **15**, 11385–11395 (2007).

¹²R. Watt, C. Kaminski, and J. Hult, in *Conference on Lasers and Electro-Optics*, San Jose, CA, 2008.

¹³C. Kaminski, R. Watt, A. Elder, J. Frank, and J. Hult, *Appl. Phys. B* **92**, 367–378 (2008).

¹⁴J. Song, Y. Hong, G. Wang, and H. Pan, *Appl. Phys. B* **112**, 529–537 (2013).

¹⁵W. Cai and C. F. Kaminski, *Appl. Phys. Lett.* **104**, 034101 (2014).

¹⁶K. Sun, “Utilization of multiple harmonics of wavelength modulation absorption spectroscopy for practical gas sensing,” Ph.D. dissertation (Stanford University, 2013).

¹⁷W. Zeller, L. Naehle, P. Fuchs, F. Gerschuetz, L. Hildebrandt, and J. Koeth, *Sensors* **10**, 2492–2510 (2010).

¹⁸W. Ren, “Mid-infrared laser diagnostics for chemical kinetics study of oxygenates,” Ph.D. dissertation (Stanford University, 2013).

¹⁹J. A. Silver, *Appl. Opt.* **31**, 707–717 (1992).

²⁰J. Reid and D. Labrie, *Appl. Phys. B* **26**, 203–210 (1981).

²¹H. Li, “Near-infrared diode laser absorption spectroscopy with applications to reactive systems and combustion control,” Ph.D. dissertation (Stanford University, 2007).

²²L. C. Philippe and R. K. Hanson, *Appl. Opt.* **32**, 6090–6103 (1993).

²³G. Rieker, J. Jeffries, R. Hanson, T. Mathur, M. Gruber, and C. Carter, *Proc. Combust. Inst.* **32**, 831–838 (2009).

²⁴W. Cai, D. J. Ewing, and L. Ma, *Appl. Math. Comput.* **217**, 5754–5767 (2011).

²⁵W. Cai and L. Ma, *Appl. Opt.* **49**, 601–610 (2010).

²⁶W. Cai and L. Ma, *Comput. Phys. Commun.* **181**, 11–16 (2010).

²⁷W. Cai, D. J. Ewing, and L. Ma, *Comput. Phys. Commun.* **179**, 250–255 (2008).

²⁸W. Zhao, C. Zhang, and C. Chen, *Proc. Combust. Inst.* **33**, 1347–1353 (2011).

²⁹P. C. Hansen, *SIAM Rev.* **34**, 561–580 (1992).

³⁰L. Ma and W. Cai, *Appl. Opt.* **47**, 4186–4192 (2008).

³¹W. Ren, A. Farooq, D. Davidson, and R. Hanson, *Appl. Phys. B* **107**, 849–860 (2012).